

The XMM deep survey in the CDF-S

X. X-ray variability of bright sources

S. Falocco¹, M. Paolillo^{2,3,4}, A. Comastri⁵, F. J. Carrera⁶, P. Ranalli⁷, K. Iwasawa^{8,9}, I. Georgantopoulos¹⁰,
C. Vignali¹¹, and R. Gilli⁵

¹ KTH, Department of Physics, and the Oscar Klein Centre, AlbaNova, 106-91 Stockholm, Sweden
e-mail: falocco@kth.se

² University Federico II, Physics Department, via Cintia, 80126 Naples, Italy

³ INFN Napoli, via Cintia, 80126 Naples, Italy

⁴ Agenzia Spaziale Italiana Science Data Center, via del Politecnico, 00133 Roma, Italy

⁵ INAF Osservatorio Astronomico di Bologna, via Gobetti 93/3, 40129 Bologna, Italy

⁶ Instituto de Física de Cantabria (CSIC-UC), Avenida de los Castros, 39005 Santander, Spain

⁷ Lund Observatory, Department of Astronomy and Theoretical Physics, Lund University, Box 43, 22100 Lund, Sweden

⁸ Institut de Ciències del Cosmos (ICCUB), Universitat de Barcelona (IEEC-UB), Martí i Franquès, 1, 08028 Barcelona, Spain

⁹ ICREA, Pg. Lluís Companys 23, 08010 Barcelona, Spain

¹⁰ Institute of Astronomy and Astrophysics, National Observatory of Athens, Palaia Penteli, 15236 Athens, Greece

¹¹ University of Bologna, Department of Physics and Astronomy, via Gobetti 93/2, 40129 Bologna, Italy

Received 5 August 2017 / Accepted 29 September 2017

ABSTRACT

Aims. We aim to study the variability properties of bright hard X-ray selected active galactic nuclei (AGN) in the redshift range between 0.3 and 1.6 detected in the *Chandra* Deep Field South (XMM-CDFS) by a long (~3 Ms) XMM observation.

Methods. Taking advantage of the good count statistics in the XMM CDFS, we search for flux and spectral variability using the hardness ratio (HR) techniques. We also investigate the spectral variability of different spectral components (photon index of the power law, column density of the local absorber, and reflection intensity). The spectra were merged in six epochs (defined as adjacent observations) and in high and low flux states to understand whether the flux transitions are accompanied by spectral changes.

Results. The flux variability is significant in all the sources investigated. The HRs in general are not as variable as the fluxes, in line with previous results on deep fields. Only one source displays a variable HR, anti-correlated with the flux (source 337). The spectral analysis in the available epochs confirms the steeper when brighter trend consistent with Comptonisation models only in this source at 99% confidence level. Finding this trend in one out of seven unabsorbed sources is consistent, within the statistical limits, with the 15% of unabsorbed AGN in previous deep surveys. No significant variability in the column densities, nor in the Compton reflection component, has been detected across the epochs considered. The high and low states display in general different normalisations but consistent spectral properties.

Conclusions. X-ray flux fluctuations are ubiquitous in AGN, though in some cases the data quality does not allow for their detection. In general, the significant flux variations are not associated with spectral variability: photon index and column densities are not significantly variable in nine out of the ten AGN over long timescales (from three to six and a half years). Photon index variability is found only in one source (which is steeper when brighter) out of seven unabsorbed AGN. The percentage of spectrally variable objects is consistent, within the limited statistics of sources studied here, with previous deep samples.

Key words. X-rays: general – galaxies: nuclei

1. Introduction

Active galactic nuclei (AGN) are characterised by strong variability at all wavelengths (e.g. [Edelson et al. 1996](#)). Rapid X-ray variability is a distinctive property of AGN and provides the most compelling evidence of super massive black holes (SMBH) at their centres ([Rees 1984](#)). The observed variability can be purely in flux or also in spectral shape; while the former is the most common, it is also possible to observe changes in the spectra, sometimes correlated with the flux variations.

Studies of the spectral variability of nearby AGN found that the AGN spectra are steeper when brighter (e.g. [Nandra et al. 1997](#)): the primary power law becomes softer when the source

brightens due to changes in the central engine ([Zdziarski et al. 2003](#)), specifically to transitions between accretion disc states. This trend has been confirmed in a sample of nearby AGN monitored regularly by the *Rossi* X-ray Timing Explorer and explained by a model where a main power-law component, intrinsically variable in flux and in slope, is combined with a constant reflection component ([Sobolewska & Papadakis 2009](#)). These findings seem consistent with a scenario where the spectral changes are due to variations in the accretion rate: in the high accretion rate regime, the X-ray-emitting corona is cooled more efficiently by the seed photons from the accretion disc, thus resulting in a higher overall flux but also a steeper power law. Recent works have shifted from spectral variability to time

lags between different spectral components. These studies found a delay between the relativistic reflection in the accretion disc and the primary continuum observed in the X-rays due to the light travel time from the corona to the reflecting accretion disc (Zoghbi et al. 2012).

In some AGNs, the origin of the observed X-ray variability has been traced back to variations in the absorbing column density along the line of sight, occurring in the torus or in the broad line region (BLR). This mechanism has been proposed to explain the X-ray variability of nearby AGN in Risaliti et al. (2002), Malizia et al. (1997), Puccetti et al. (2004), and Risaliti et al. (2010), where significant changes in the column densities of the X-ray absorber have been reported. This suggests that the absorbing torus has a clumpy structure and that the observed variability is partly due to orbiting clouds in the line of sight. The timescale of this variability goes from days to months. A similar result has been found by Torricelli-Ciamponi et al. (2014) in a larger sample of AGNs, showing that occultations by the BLR may be the responsible for part of the observed variability above 2 keV over timescales of days.

Studies of the X-ray variability in high redshift AGNs have confirmed that flux variability is typical of these sources over timescales of months to years (e.g. Bauer et al. 2003; Paolillo et al. 2004; Papadakis et al. 2009; Shemmer et al. 2014; Lanzuisi et al. 2014; Vagnetti et al. 2016). The variability timescales explored so far have been extended to decades in Middei et al. (2017). However, few of these works have been able to investigate in detail the spectral variability of their sources, mainly due to the low statistics: spectral variability has been found in the ensemble analyses presented by Gibson & Brandt (2012) and Serafinelli et al. (2017). Paolillo et al. (2004), studying the *Chandra* Deep Field South (CDFS), found evidence for intrinsic flux variability for the majority of the sample but spectral variability was observed in only ~30% of the sources. Half of the spectrally variable sources show an anti-correlation between hardness ratio (HR) and flux, a behaviour compatible with the softer-when-brighter trend discussed above. A similar result was found in Mateos et al. (2007), who found 80% of the sources to be variable in flux in the Lockmann Hole and only 40% of sources variable in X-ray colours at 3σ level. Furthermore, Shemmer et al. (2014) found a high redshift source ($z = 2.7$) with significant spectral variability that they argued was due to a variable column density in the line of sight. More recently, Yang et al. (2016) studied the CDFS dataset finding variability in X-ray luminosity in 74% of the AGN in the survey. They detect variability in column densities in only 16% of their AGN sample.

Taking advantage of the good count statistics in the *XMM-Newton* observation of the *Chandra* Deep Field South (XMM CDFS, Comastri et al. 2011), we aim at exploring the flux and spectral variability in AGN, checking the previously described pictures. For this purpose, we investigate the ten brightest sources in the XMM CDFS. The main purpose is to understand what is the principal driver of the variability of high redshift sources, investigating the variability of several spectral components: photon index of the primary power law, column densities, and reflection. The spectra have been analysed with Xspec version 12.9. The errors correspond to a 90% confidence level for one interesting parameter ($\Delta\chi^2 = 2.71$) where not otherwise stated. The cosmological parameters are the default ones in Xspec: $H_0 = 70 \text{ km s}^{-1} \text{ Mpc}^{-1}$, $\Omega_\Lambda = 0.73$, $\Omega_{\text{tot}} = 1$ (Komatsu et al. 2011).

2. Source sample and data analysis strategy

2.1. The data

This work is based on an observation of the *Chandra* Deep Field South with *XMM-Newton* for a total of 3.3 Ms of full exposure time (hereafter, the sample is called XMM CDFS). The cleaned exposure times from the EPIC pn (p-type n-type junction semiconductor) and MOS (Metal Oxide Semiconductor) cameras are 2.5 Ms and 2.8 Ms respectively. The XMM CDFS has 33 observations obtained in two distinct periods, 2001–2002 and 2008–2009. The details on the data reduction and the source detection are presented in Ranalli et al. (2013).

Despite the larger sensitivity of the EPIC pn detector, a comparison of the background levels of the MOS and pn (see Ranalli et al. 2013) shows that the background of the MOS camera is always lower and more stable than the pn. In addition, the number of sources falling in the gaps of pn CCD (charge coupled devices) is larger than for the MOS detectors, due to their different geometry, thus making it more challenging to extract consistent lightcurves and spectra over several years for sources close to CCD gaps where the background contribution is hard to estimate properly (Ranalli et al. 2013). We thus choose to limit our analysis to the MOS data.

The 33 observations are grouped into six main intervals: July 2001, January 2002, July 2008, January 2009, July 2009, and January–February 2010 (see Table 3 of Iwasawa et al. 2015). We note that there are inhomogeneities in the lightcurve sampling because the dead MOS1 CCD (Ranalli et al. 2013) affects the sampling of sources in different positions of the field of view due to the variable aim point of the observations and roll angles. The background level of the observations has increased over time, being lower in the 2001–2002 observations than at later epochs (Ranalli et al. 2013) while, on the other hand, the first epoch is composed of less observations than the following ones, and thus has a smaller overall exposure time. These effects raise the uncertainties on the spectral parameters of the six epochs.

2.2. The sample

This work focuses on the ten AGN in the 2–10 keV catalogue published by Ranalli et al. (2013) defined as having more than 5000 time-integrated counts in the source detection band, 2–10 keV observed frame band. The ten AGN have spectroscopic redshifts from 0.3 to 1.9 (from Treister et al. 2009; Silverman et al. 2010; Szokoly et al. 2004; Luo et al. 2017) and five of them have an optical spectroscopical classification from the literature. Sources with id. 319, 337, and 203 (the identification numbers refer to the catalogue of Ranalli et al. 2013) are classified as broad line AGN by Szokoly et al. (2004). Source 33 is classified as an unabsorbed AGN in the optical spectroscopic study presented in Treister et al. (2009); source 48 is classified as a narrow emission line galaxy in Silverman et al. (2010).

The variability of sources 203 and 319 has been studied previously in Iwasawa et al. (2015), but here we include them because we use a different approach, and also to check the consistency of our results; sources 33 and 48 have been described as absorbed sources from the properties of their integrated spectra in Iwasawa et al. (2012) and in Georgantopoulos et al. (2013) respectively; source 352 has been studied by Vignali et al. (2015) who found features from an outflowing wind in the integrated spectrum. Table 1 summarises the properties of the ten AGN.

Table 1. Source properties.

Source	Coord.	z	C	P	NXV	NXV_c	L	f_{LC}	f_{epochs}
(1)	(2)	(3)	10^3 (4)	(5)	10^{-2} (6)	10^{-2} (7)	10^{44} erg/s (8)	% (9)	% (10)
203	03:32:08.62 –27:47:34.80	0.544	46.0	1	2.55 ± 0.64	2.83	1.30 ± 0.03	17	11
319	03:32:26.95 –27:41:06.00	0.742	35.5	1	3.07 ± 0.62	3.51	3.24 ± 0.04	19	13
358	03:32:07.85 –27:37:32.16	0.976	17.8	1	2.99 ± 1.58	3.52	1.4 ± 0.5	19	10
337	03:32:38.14 –27:39:44.64	0.837	11.2	1	3.77 ± 0.77	4.36	1.67 ± 0.04	21	23
359	03:32:11.54 –27:37:27.84	1.574	6.9	1	4.15 ± 0.94	5.20	5.35 ± 0.18	23	18
292	03:32:48.05 –27:42:33.12	0.979	5.5	1	3.46 ± 0.96	4.08	0.91 ± 0.15	20	15
33	03:33:01.70 –27:58:18.84	1.843	4.0	1	2.38 ± 0.92	3.06	9.2 ± 0.3	18	18
382	03:32:28.32 –27:35:35.88	0.527	2.5	1	12.7 ± 3.7	14.06	0.59 ± 0.06	38	28
48	03:32:38.93 –27:57:00.72	0.298	2.3	1	1.51 ± 0.49	1.61	0.07 ± 0.03	13	16
352	03:32:42.46 –27:38:15.72	1.6	1.5	0.99	2.90 ± 1.81	3.65	1.23 ± 0.60	19	12

Notes. The table lists: (1) source IDs, (2) coordinates, (3) spectroscopic redshifts, (4) net integrated counts in 0.5–7 keV rest-frame bands from MOS1 and MOS2 instruments, (5) variability probability combined from MOS1 and MOS2 ($1 - [(1 - P_{MOS1}) \times (1 - P_{MOS2})]$), (6) excess variance (weighed over the errors) of MOS1 and MOS2, (7) excess variance corrected for redshifts, (8) continuum luminosity in the 0.5–7 keV rest-frame band (average between the high- and low-state spectra, from the best fits in Table 2), (9) fractional flux variability from the lightcurves, (10) fractional variability in the power-law normalisations in the spectra of the available epochs.

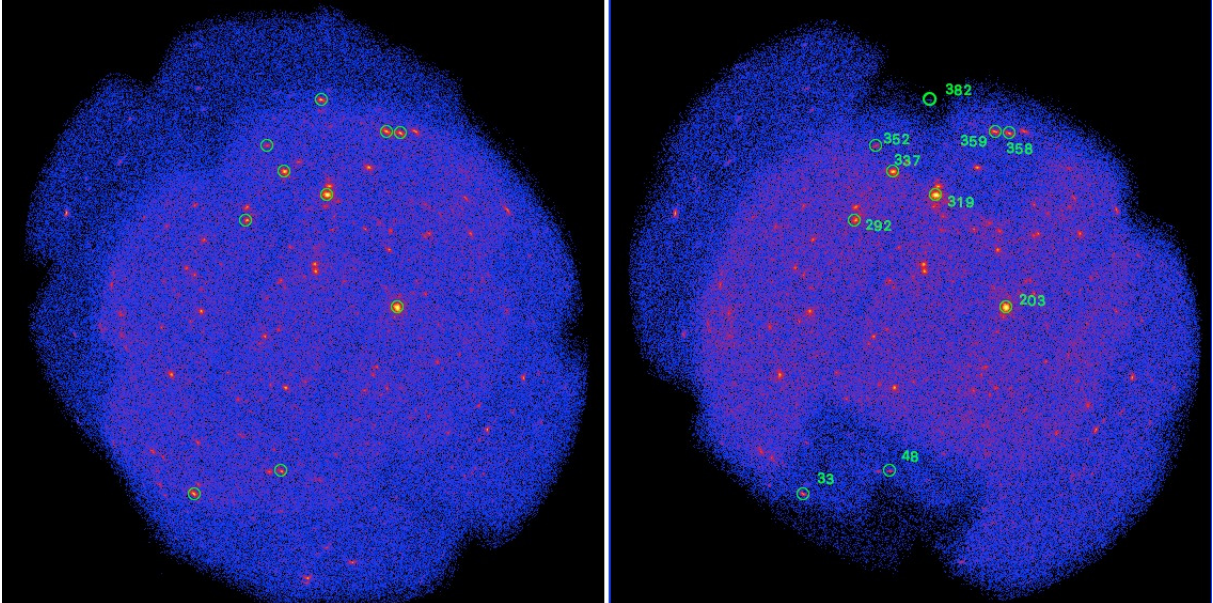


Fig. 1. Spatial distribution of the sources investigated in this study overlaying on the stacked MOS1 (right hand panel)/MOS2 (left hand panel) field of view (in the 0.5–8 keV band).

The position of the sources within MOS1 and MOS2 field of view are displayed in Fig. 1.

2.3. Analysis strategy

In this context our work explores the spectral variability of the CDFS sources using an approach that combines lightcurves, HRs, and spectral analysis, investigating both individual epochs as well as the combined spectra of the high and low states (see below), in order to constrain the origin of the flux variability and its connection with the primary emission mechanisms. As a starting point we extract the flux lightcurves of each source separately for the MOS1 and MOS2 detectors, in the 0.5–8 keV observed frame band, binning the data in individual observations. The lightcurves are shown in the top panels of Figs. 2–12, where it can be noted that the data points are, on average, consistent

between the MOS1 and MOS2. The points where the measured fluxes differ significantly are usually due to source positions at the edge of the FOV (field of view) or close to the chip gaps where the exposure corrections are more uncertain. We thus compute for each epoch the average of the fluxes from the two cameras (the average is weighted with the errors), as the best estimate of the intrinsic single-epoch flux. The six panels in the figures refer to the six epochs mentioned earlier and defined in Iwasawa et al. (2015). We assess if a source is variable based on a comparison with 1000 simulations of each lightcurve in each detector (Paolillo et al. 2004); we assume a constant flux set to the average source and background flux of the real source. We characterise the source variability through the normalised excess variance (NXV) for each lightcurve (Nandra et al. 1997; Turner et al. 1999; Edelson et al. 2002). We then take into account the different lengths of the lightcurves in their rest-frame applying the correction for redshifts as explained in

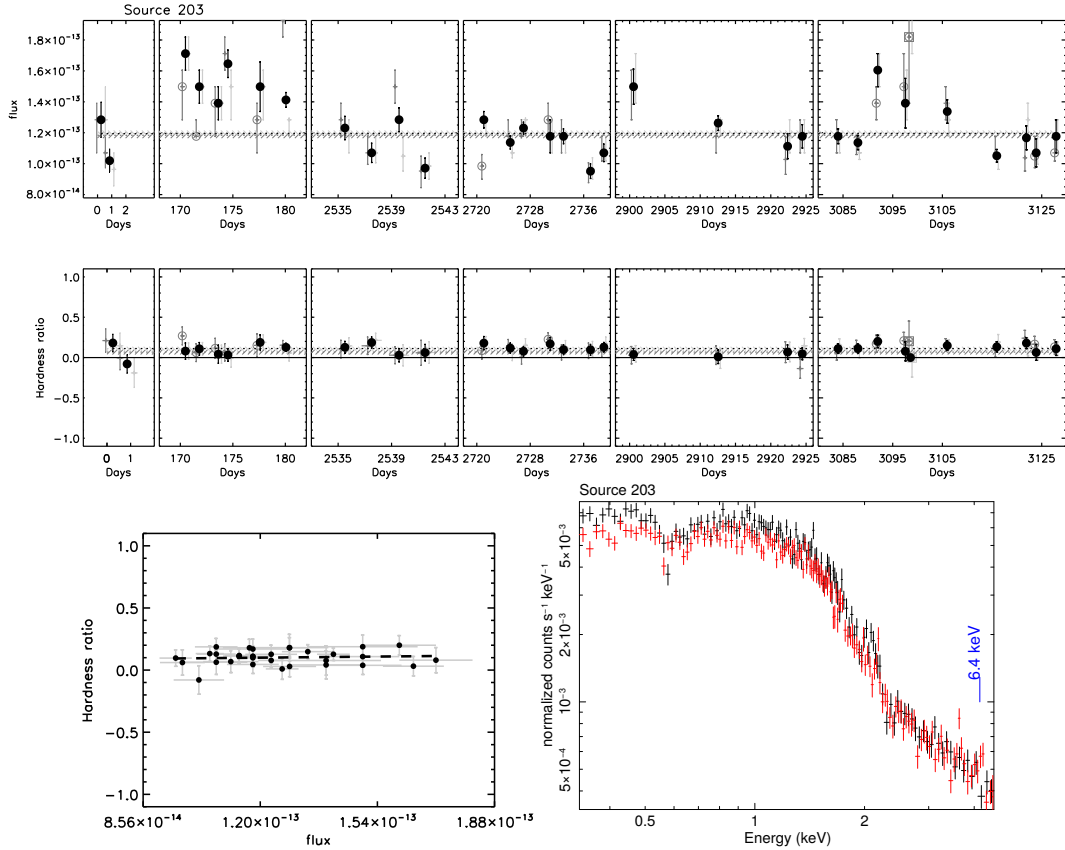


Fig. 2. *First and second rows:* lightcurves in fluxes and HR. The fluxes are computed in the 0.5 and 8 keV observed frame band averaged between MOS1 and MOS2 at each of the 33 observations following the procedure of [Park et al. \(2006\)](#). Black solid dots represent the weighted average of the two MOS detectors, where we only use epochs without any potential problem in the photometry. Observations with potential photometry problems (e.g. where either more than 10% of the source area falls outside one of the MOS chips or on an intra-chip gap, or where the source and background regions fall on different chips) are represented by an empty circle; similarly observations where more than 30% of the background area falls outside one of the MOS chips or on an intra-chip gap, are represented by an empty square. These epochs have been represented in grey. The horizontal error bars represent the duration of the observation. The flux averaged over all epochs and both MOS1 and MOS2 detectors is shown as a dotted black line. Only epochs without any potential problem in photometry are used to compute the averages shown in the plot and used for the spectral analysis described in the text. The black solid line marks the zero level in all panels. The average of the MOS fluxes and HRs (over the epochs without any potential problem in the photometry) is represented as a dotted black line and its error is represented by dashed grey lines. *Third row, left:* HR versus flux of the individual observations. The dashed line is the linear regression line (calculated not considering the errors). *Third row, right:* high-flux-state and low-flux-state spectra represented with black and red data points respectively.

[Vagnetti et al. \(2016\)](#). This estimate allows a comparison of variability amplitudes between the ten sources analysed here, and with known samples in the literature.

Hardness ratio defined as $HR = \frac{F_{2-8} - F_{0.5-2}}{F_{0.5-2} + F_{2-8}}$, where $F_{0.5-2}$ and F_{2-8} are the fluxes in the 0.5–2 keV and 2–8 keV bands. Lightcurves are then constructed to investigate colour changes of the sources over the timescales explored here. The HR lightcurves are derived with the same sampling as the flux lightcurves and serve as a preliminary spectral variability assessment, to be refined through a proper spectral analysis when the statistics are sufficient. The bands are in the observed frame, so for the highest redshift sources the HR is not actually sensitive to the softest spectral features (i.e. to the N_H). For each source we further plot the HR versus flux to identify correlations between the flux and spectral variability.

In addition to the flux and HR lightcurves, we performed a more detailed spectral analysis. For this purpose, the spectra of the individual epochs were merged by grouping them in two different ways: the spectra were first grouped into the six time intervals as in [Iwasawa et al. \(2015\)](#), corresponding to the panels shown in the top row of Figs. 2–12, to check if any variability

of the spectral features is related to the sampled timescales. Subsequently, they were grouped in high and low states, the main purpose being to understand whether the flux changes correlate with spectral changes as well. The high and low flux states of MOS1 and MOS2 are defined as having flux higher and lower than the average flux level over the entire lightcurve (black dotted line in Figs. 2–12, top panel).

The merging of the MOS1 and MOS2 spectra corresponding to the same source, observation, and filter was done computing the straight sum of the counts and the exposures. The backscale of the total spectrum was computed as the average of the backscale values of the individual spectra weighted for the contribution of each exposure. The response matrix and ancillary file of the combined spectrum were constructed in the same way as the weighted average (computed using `ftools` task `addrmf`). The procedure just described was repeated for the merged spectra of the six epochs and of the high and low flux states. The background-subtracted spectra of each epoch and of the high- and low-states spectra were rebinned in order to have more than 20 counts in each bin for the χ^2 statistics to be valid. The final spectra of the ten sources have different qualities in the six epochs, ranging from ~ 100 net counts in the worst case (the

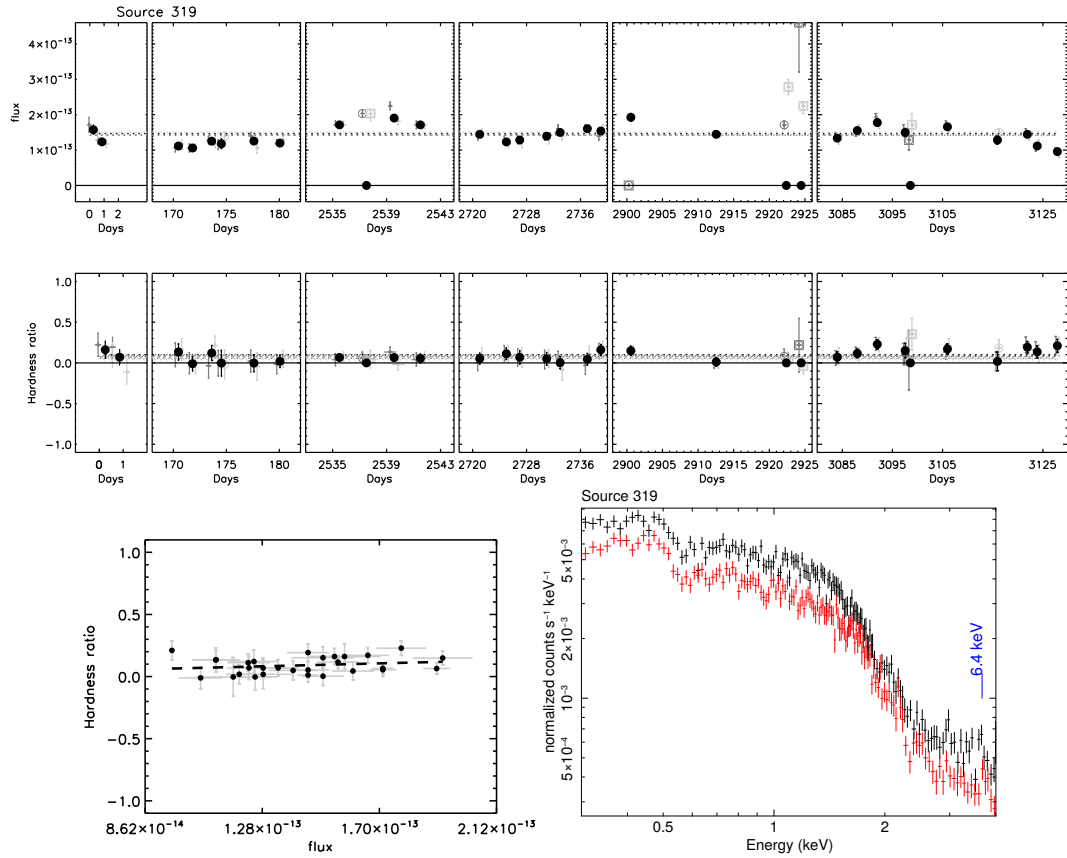


Fig. 3. Source 319. Plot panels as in Fig. 2.

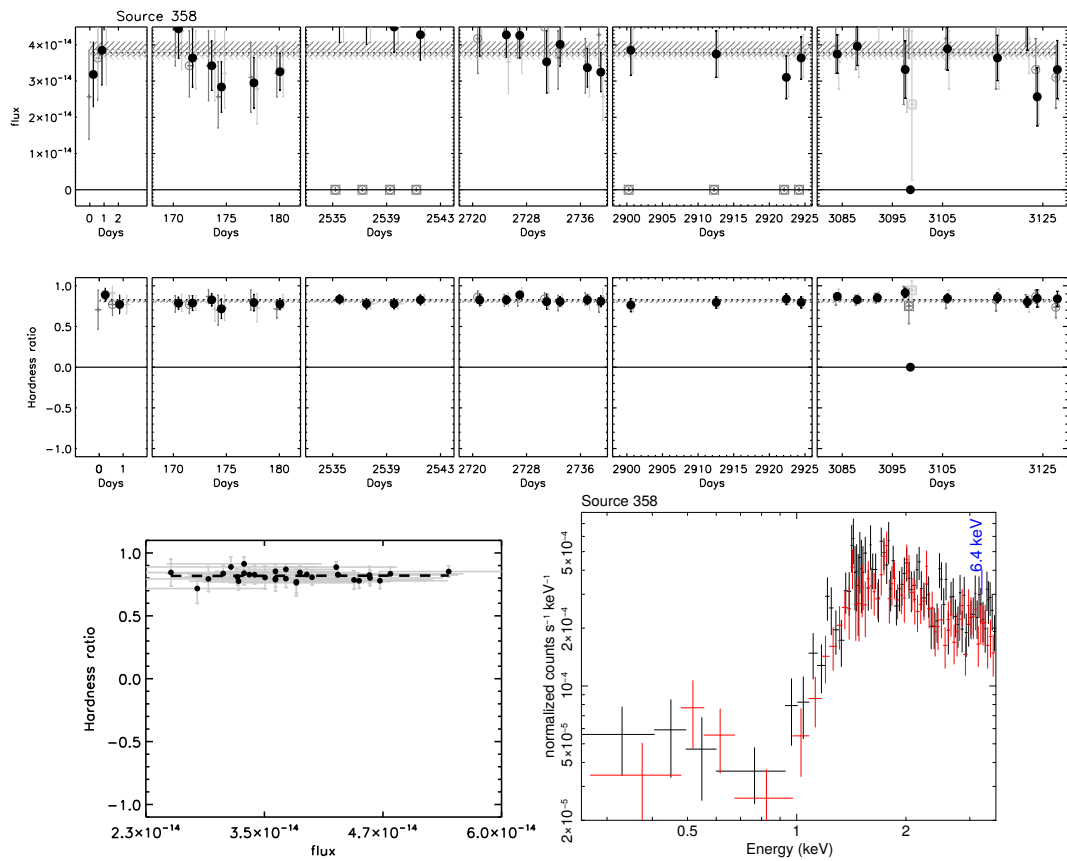


Fig. 4. Source 358. Plots as in Fig. 2.

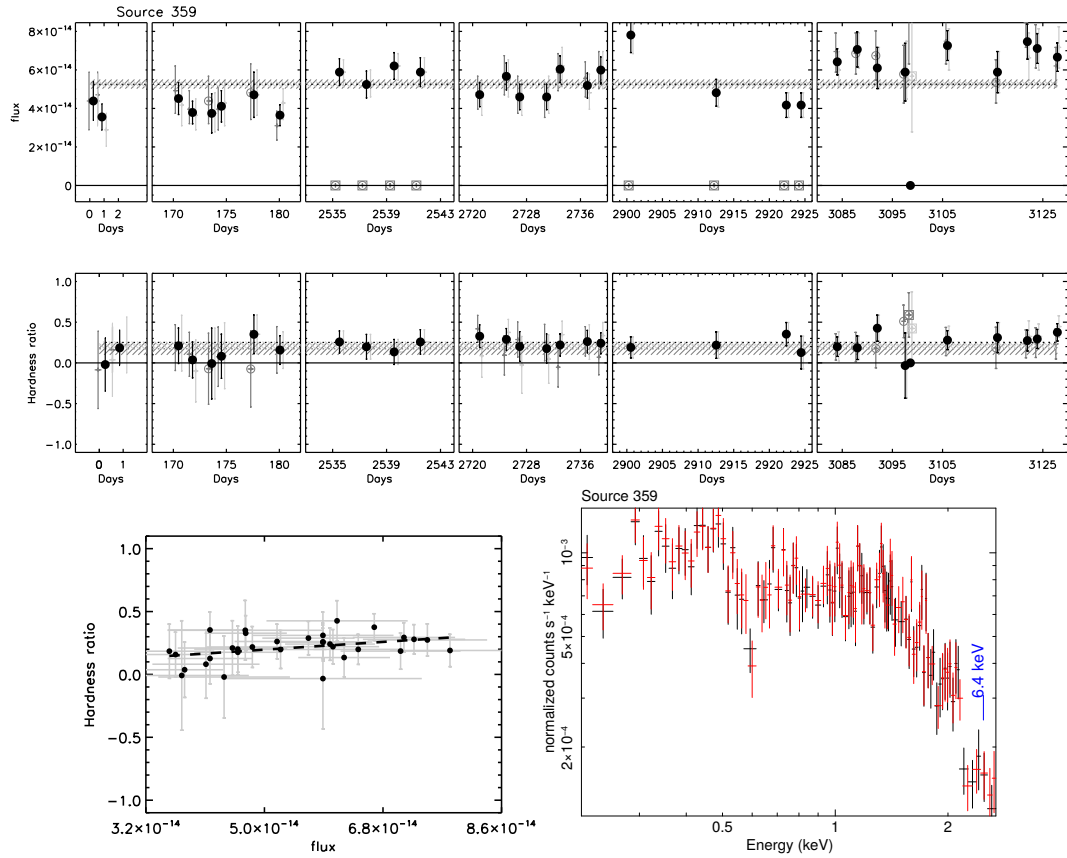


Fig. 6. Source 359. Panels as in Fig. 2.

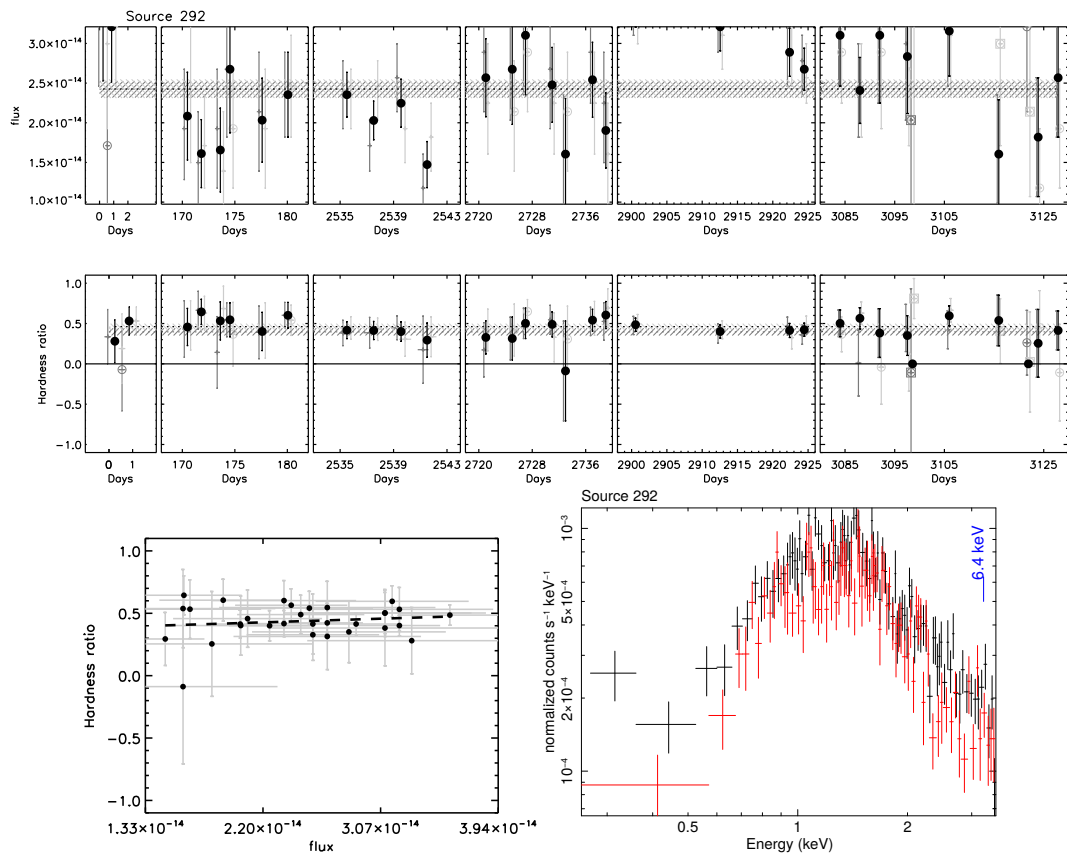


Fig. 7. Source 292. Panels are displayed as in Fig. 2.

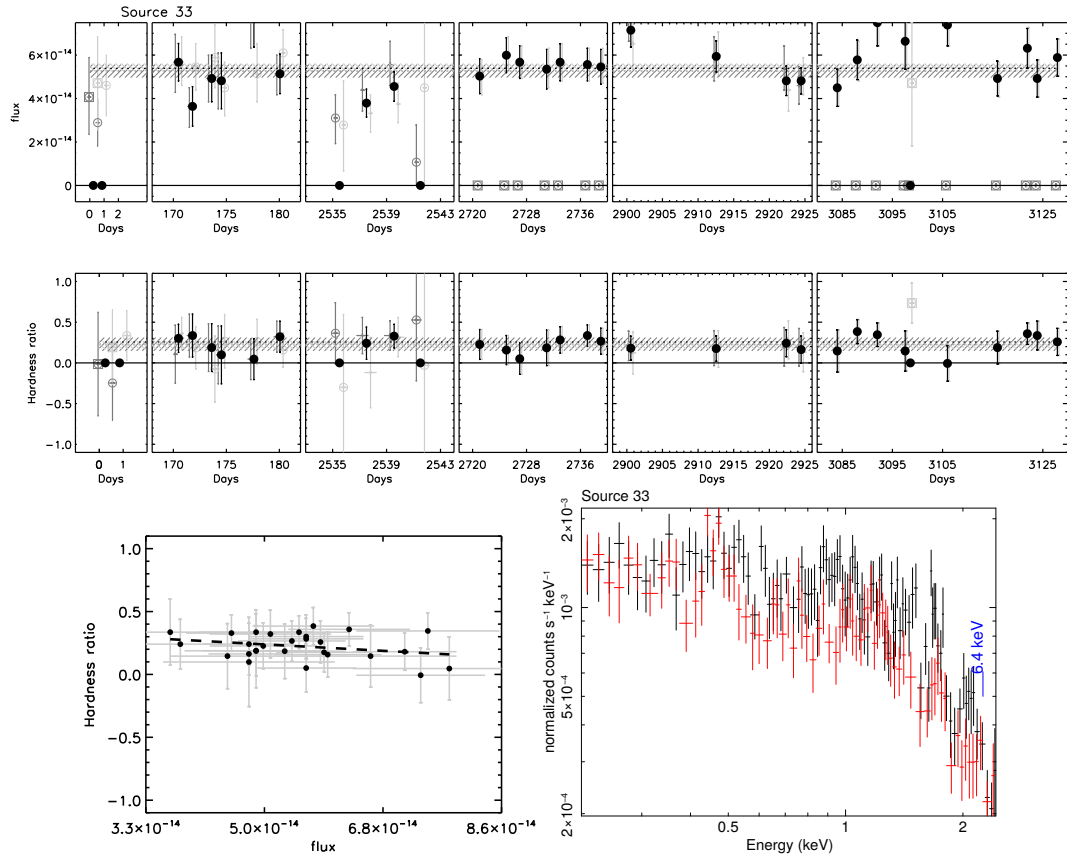


Fig. 8. Source 33. Panels displayed as in Fig. 2.

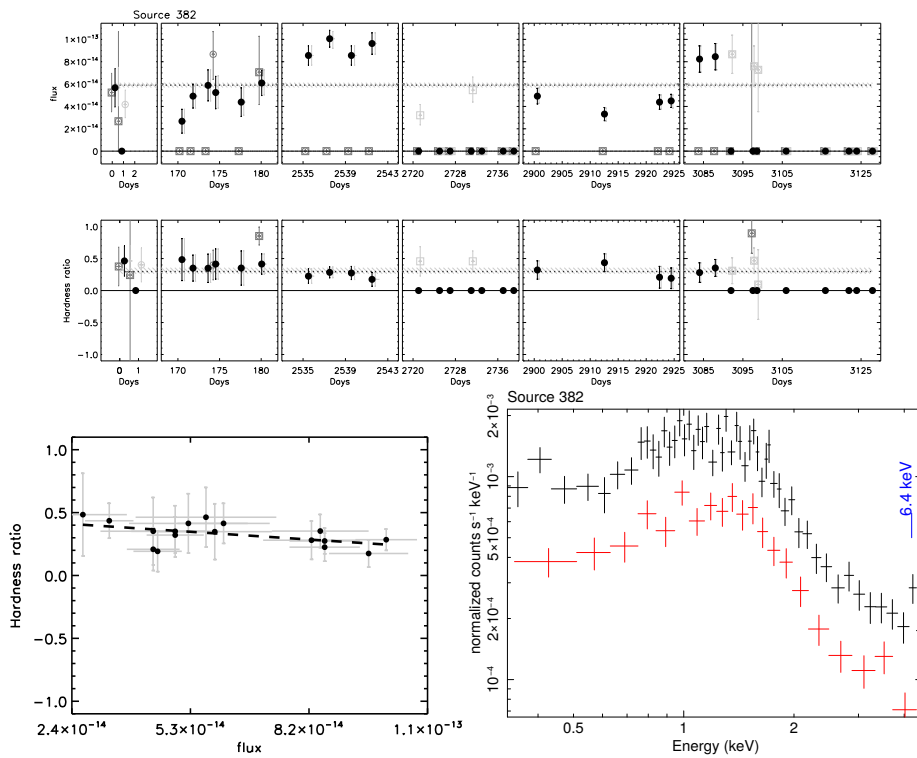


Fig. 9. Source 382. Panels as in Fig. 2.

in xspec is the first one used to fit the soft excess; it represents thermal emission (Bremstrahlung and lines), which produces lines in the soft X-rays. This thermal component is emitted from

ionised material far from the central engine. This collisional model is good in a first approximation for the narrow line region (NLR) even if it is photoionised. The fixed parameters adopted

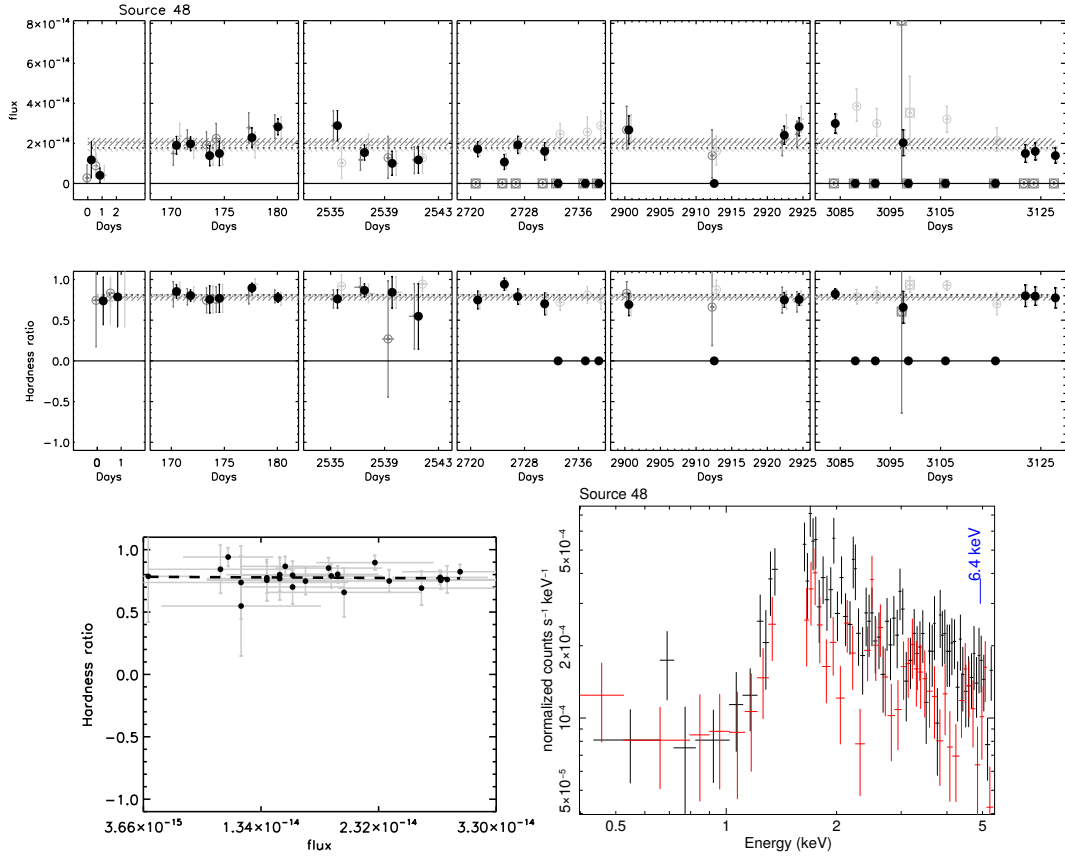


Fig. 10. Source 48. Plots as in previous figures.

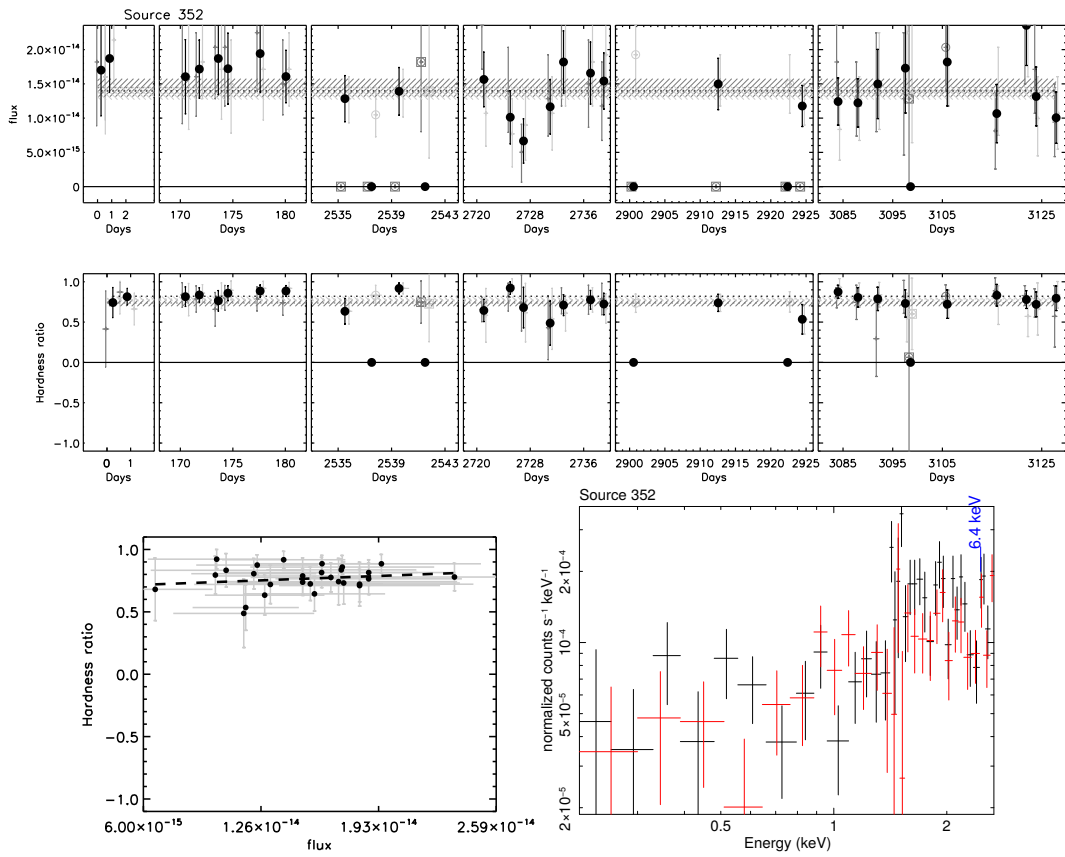


Fig. 11. Source 352. Plots as in Fig. 2.

Table 2. Fits results.

(1) Source	(2) Fit	(3) N_{H} 10^{22} cm^{-2}	(4) Γ	(5) EW eV	(6) T, E, R KeV, KeV, –	(7) $\chi^2/\text{d.o.f.}$	(8) r	(9) p
203 _h	baseline	$5.5 \pm 1.5 \times 10^{-2}$	1.97 ± 0.04	<91	–	244.06/239	–0.412	0.42
203 _l	baseline	$5.8 \pm 1.3 \times 10^{-2}$	1.94 ± 0.04	159 ± 53	–	303.20/267	–	–
319 _h	baseline	<0.007	2.04 ± 0.02	158 ± 52	–	215.00/207	–0.06	0.91
319 _l	baseline	<0.004	2.06 ± 0.02	169 ± 56	–	181.19/197	–	–
358 _h	baseline	7.2 ± 1.8	1.35 ± 0.45	<101	–	67.01/77	–0.491	0.67
358 _h	E free	8 ± 2	1.46 ± 0.50	<138	$E = 3.37 \pm 0.27$	66.02/76	–	–
358 _h	mek	7.7 ± 2.0	1.4 ± 0.5	<109	$T < 0.23$	57.79/75	–	–
358 _h	pow	9.2 ± 2.0	1.68 ± 0.47	<125	–	58.68/76	–	–
358 _l	baseline	9.7 ± 2.2	1.91 ± 0.55	<136	–	49.27/59	–	–
358 _l	mek	10.7 ± 2.6	2.1 ± 0.6	<152	$T < 0.91$	39.64/57	–	–
358 _l	pow	11.3 ± 2.1	2.18 ± 0.53	<156	–	41.90/58	–	–
337 _h	baseline	<0.01	2.23 ± 0.04	172 ± 91	–	139.55/152	0.986	0.01
337 _h	E free	<0.01	2.23 ± 0.04	239 ± 100	$E = 3.59 \pm 0.07$	133.91/151	–	–
337 _l	baseline	<0.05	2.18 ± 0.07	310 ± 159	–	107.66/112	–	–
359 _h	baseline	<0.05	1.70 ± 0.08	<80	–	121.24/108	–0.907	0.28
359 _l	baseline	<0.06	1.69 ± 0.09	<97	–	119.52/108	–	–
292 _h	baseline	0.78 ± 0.20	1.40 ± 0.16	<84	–	140.00/135	0.26	0.67
292 _h	mek	1.04 ± 0.30	1.54 ± 0.20	<108	$T = 0.219 \pm 0.090$	130.63/133	–	–
292 _h	pow	1.49 ± 0.50	1.64 ± 0.24	<124	–	132.32/134	–	–
292 _l	baseline	1.1 ± 0.3	1.58 ± 0.22	<141	–	101.01/104	–	–
33 _h	baseline	<0.04	1.80 ± 0.07	<138	–	110.20/116	–0.99	0.08
33 _h	Efree	<0.05	1.82 ± 0.08	93 ± 60	$E = 2.1 \pm 0.1$	106.68/115	–	–
33 _l	baseline	<0.14	1.87 ± 0.10	155 ± 92	–	83.91/101	–	–
33 _l	Efree	<0.13	1.87 ± 0.20	190^{+800}_{-110}	$E = 2.31 \pm 0.20$	83.09/100	–	–
382 _h	baseline	0.15 ± 0.06	1.64 ± 0.13	<226	–	70.76/74	–	–
382 _l	baseline	0.19 ± 0.10	$1.66^{+0.20}_{-0.18}$	<187	–	24.11/39	–	–
48 _h	baseline	2.32 ± 0.60	1.41 ± 0.32	158 ± 150	–	82.93/70	0.813	0.39
48 _h	mek	2.6 ± 0.6	1.48 ± 0.32	172 ± 142	$T = 0.71 \pm 0.20$	66.9/68	–	–
48 _h	pow	3.2 ± 0.8	1.62 ± 0.35	194 ± 150	–	72.33/69	–	–
48 _h	pex	4.3 ± 1.0	2.48 ± 0.30	144 ± 140	$R > -1$	71.85/68	–	–
48 _h	pex Efree	4.3 ± 1.0	2.48 ± 0.30	148 ± 138	$R > -0.4, E = 4.89 \pm 0.20$	71.54/67	–	–
48 _l	baseline	1.5 ± 0.9	1.03 ± 0.50	<211	–	60.07/44	–	–
48 _l	mek	3.6 ± 2.0	1.5 ± 0.7	<275	$T < 6$	47.92/42	–	–
48 _l	pow	3.7 ± 1.5	1.59 ± 0.54	<304	–	47.61/43	–	–
48 _l	pex	3.7 ± 1.5	1.59 ± 1.00	<303	$R > -0.25$	47.56/42	–	–
48 _l	pex Efree	3.7 ± 1.4	1.6 ± 1.6	92^{+300}_{-30}	$R > -0.25, E = 4.56^{+0.80}_{-0.04}$	43.4/41	–	–
352 _h	baseline	8.2 ± 3.5	<1.1	<180	–	72.20/34	–0.924	0.25
352 _h	pex	25 ± 6	1.72 ± 0.20	<178	$R > -0.25$	41.18/32	–	–
352 _l	baseline	<2.6	<0.7	419 ± 200	–	31.77/26	–	–
352 _l	pex	51 ± 10	<1.4	<1000	$R > -1$	18.77/24	–	–

Notes. Column 1: source ID; Col. 2: fitting model in the 0.5–7. keV rest-frame band: baseline (absorbed power law and a gaussian), E free (baseline with Energy of gaussian free), mek (baseline+mekal) to account for the soft excess, pex (baseline+pexrav), pex E free (baseline+pex with centroid of the gaussian free), pow: baseline+pow to account for the soft excess; Col. 3: column density of local absorber in 10^{22} cm^{-2} ; Col. 4: photon index of the observed power law; Col. 5: EW of the narrow Fe line at 6.4 keV expressed in eV; Col. 6: temperature of material emitting the mekal component (mek); Col. 6 represents the centroid energy of the iron line when left free and the reflection fraction of the Compton reflection when added; Col. 7: chi square/d.o.f.; Col. 8: linear correlation coefficients obtained with the least-squares regression between photon index and the flux (obtained from the spectral fits of the six epochs in the band between 0.5–7. keV); Col. 9: p -value for the least-squares regressions reported in Col. 8: these represent the probability that the two parameters are not correlated. In Cols. 8 and 9, the least-squares regressions have not been computed for source 382 (because it has only the spectra of two epochs).

for the mekal model are the hydrogen density $n_{\text{H}} = 1 \times \text{cm}^{-3}$ and the metal abundance = 1 (solar abundance). The temperature is free to vary during the fitting. A second attempt to fit the soft excess has been made considering Compton up-scattering of the photons from the disc, represented by an additional power-law

component added to the baseline model. We fixed its slope to that of the primary power law and kept the normalisation as a free parameter.

For two more sources (48, 352) the data suggest the presence of a Compton reflection component. We model this contribution

through the *pexrav* model, set up to represent the reflected component only (the direct one is already accounted for by the power law of the baseline model). The values of the abundances have been fixed to solar values, the angle to 45° , and the cutoff energy to 100 keV. Since the slope of the reflected component should be the same as the primary power law, we fixed their photon indices to the same value.

3. Results and discussion

We investigated the spectra of the sources to get more detailed information than the HR study. Some studies propose an interpretation of the AGN X-ray variability in scenarios similar to Galactic black holes but scaled by the BH (black hole) masses, so it is characterised by larger timescales in AGN (from months to years, following McHardy et al. 2006). In particular, Papadakis et al. (2009) and Sobolewska & Papadakis (2009) found a correlation between the observed flux variability and the spectral properties in AGN. In these works they reported an intrinsic difference in the power-law slopes due to a varying accretion rate in each source. In fact, the power law is produced through inverse Compton scattering by a corona close to the disc. The dissipation of the corona strongly depends on the geometry of the system and it is inversely proportional to the accretion rate \dot{m} in the geometry described by Esin et al. (1997). In this scenario, the efficiency of the coronal cooling will be proportional to \dot{m} as well as to the slope of the primary power law in the X-rays. As proposed by Esin et al. (1997), disc transitions from “low” to “high” states are the reason for the observed variability in the X-ray binaries. As \dot{m} increases, the inner radius of the accretion disc approaches the SMBH, the primary radiation (soft X-rays) impinging on the corona is higher, the coronal cooling is more efficient, and the X-ray primary continuum spectrum will be steeper as described in Zdziarski et al. (1999). In the “high” state, the disc is extended down to regions very close to the SMBH and $\dot{m} > 1$. The term “low” state, instead, refers to a truncated disc and $\dot{m} < 1$. In this case, the thermal emission from the accretion disc will be lower, the corona cooling will be less efficient, and the power-law continuum will be harder (Zdziarski et al. 1999). This kind of variability can occur over a variety of timescales, from minutes to months (Belloni et al. 1997; Fender & Belloni 2004) for the binaries; the variability timescales are scaled with the BH masses and luminosities following McHardy et al. (2006)’s empirical relation, so they are typically longer for AGN (from months to years) and detectable in the monitoring baseline of the XMM CDFS.

3.1. Lightcurves in fluxes and in hardness ratios

Our photometric analysis shows that all the sources investigated here show significant flux variability with a confidence level $\geq 99\%$ (Table 1). The lowest probability is found for the faintest source (i.e. source 352), in agreement with the expectation that all AGNs are intrinsically variable and only the data quality prevents us from detecting variability at low fluxes (see e.g. Paolillo et al. 2004; Young et al. 2012; Yang et al. 2016). The measured excess variance NXV spans values between 0.01 and 0.1, corresponding to flux variations in the range 13–38% over timescales between three and six and a half years (at rest-frame), in agreement with what is observed in previous studies of the CDFS (Paolillo et al. 2004, 2007, 2017). We did not find any strong anti-correlation between variability (NXV) and the X-ray luminosity (found for example in Almaini et al. 2000;

Paolillo et al. 2004; Lanzuisi et al. 2014; Yang et al. 2016); however, this is not surprising because we probe a relatively narrow range of luminosities and also because, in order to measure such a trend, we would need multiple lightcurves of the same source or a larger sample of sources with similar properties (Allevato et al. 2013; Vaughan et al. 2003).

The HR lightcurves show that the flux variability does not correspond to a significant X-ray colour variability because the HR do not vary across the individual epochs in the majority of the sources (see second row of Figs. 2 to 12). To understand this result, we first underline that the sensitivity to the HR variability is strongly dependent on the data quality, since the limited counts statistics may prevent us from detecting it (as pointed out also in Paolillo et al. 2004 and Mateos et al. 2007). This explains, at least in part, why the HR variability is common in nearby AGN characterised by spectra with good counts statistics (Papadakis et al. 2009). On the other hand, a larger sample size would certainly increase the chance of finding spectrally variable sources; for example, the percentage was 30% in the larger sample constructed from the previous CDFS by Paolillo et al. (2004). HR variability has been also found in $20 \pm 6\%$ of the 123 brightest AGNs in the LH (Lockman Hole) field (Mateos et al. 2007). Mateos et al. (2007) point out that this fraction increases with the quality of data, and can potentially reach up to 40%.

In the Comptonisation scenario discussed above, the HR is expected to anti-correlate with flux, since in the bright states the seed photons cool the corona thus softening the spectrum. We looked for evidence of such behaviour in our sample, but a large scatter in the HR versus flux trend and the large uncertainties in the two quantities prevent us from clearly detecting such a trend. Having said that, a marginal decrease of the HR with the flux can be barely seen in sources 337, 382, and 33. Only for source 337 is a spectral steepening with the increasing flux confirmed by the spectral analysis described below. On the other hand, clear evidence for a spectral hardening with the increasing flux is not found in any of our sources. Our results are generally in agreement with the finding that this sample does not display a significant spectral variability for the majority of the sources, except for source 337 that instead agrees with the “steeper when brighter trend”. While it is possible that the limited spectral variability observed here is a consequence of the limited spectral quality in the individual observations and of the limited sample size, it is also possible that the changes in the spectral components are more complex than a simple HR analysis can reveal on an epoch-to-epoch basis. We thus investigate the sources in more detail through temporal-resolved spectral analysis. We point out that the large HR found for sources 358, 48, and 352 already suggest the presence of a hard (reflection) component, which is confirmed by the improved spectral analysis discussed below.

3.2. Time-resolved spectral analysis

The single-epoch spectra have been first fitted with the baseline model to look for variations in the spectral components, focusing on the power-law normalisation and slope, amount of absorption, and iron line properties. We first assessed if there is variability in the power-law normalisations, finding that, across the six epochs, it goes from 10% from the source where it is less variable (358) to 28% for source 382, as can be seen in Table 1. In general, the power-law slopes’ variability is not as strong as the flux variability, since the power-law slopes vary at most by 15% across the six epochs (in sources 203 and 337). To check whether the results found for local AGN can be extended to our

sample, we explored the trends between power-law slopes and continuum fluxes that in [Sobolewska & Papadakis \(2009\)](#) are anti-correlated. We measured the linear correlation coefficients between the power-law photon index Γ and the continuum flux, as well as the probabilities for the correlations, using the least-squares regression. Table 2 (Col. 8) shows the linear correlation coefficients (r) and the p -values (which represent the probabilities that the two measurements are not correlated, see Col. 9) obtained with the linear least-squares regression between photon indices and fluxes for the epochs where measurements of the two parameters could be derived from spectral fitting. The correlation coefficients reported in the table do not take into account the uncertainties on the measurements. Source 337 is steeper-when-brighter, confirming the trend anticipated by the HR versus flux discussed in the previous section. For sources 203 and 319 we did not find the “steeper-when-brighter” trend, in agreement with [Iwasawa et al. \(2015\)](#). For the remaining sources, we did not find clear evidence for a trend between photon index and flux; for source 382 we could not do the linear correlation due to the large uncertainties on the two measurements.

In short, the power-law slope Γ does not appear to be significantly variable for the majority of the sources, as opposed to the fluxes of the primary power laws. To test if this result is affected by changes in the absorbing column along the line of sight, we performed additional fits to the spectra in the 2–7 keV rest-frame band and confirmed that there is no significant variability in the power-law slopes, consistently with the fits in the 0.5–7 keV rest-frame band.

We tried to determine whether the absorber column density presents variability in the epochs considered but the values found for the column densities in the individual epochs are broadly compatible within the uncertainties. We also tried to study the iron line variability and we found that the EW (equivalent width) are consistent within the uncertainties across the epochs explored in this survey.

3.3. Flux-resolved spectral analysis

Since the individual epochs do not display any evident spectral variability, we merged the spectra of high- and low-flux states, defined in Sect. 2. The high- and low-state fluxes differ, on average, by about 10% in our sample. The power-law slopes are broadly consistent within the uncertainties in the high- and low-flux states’ spectral fitting. We also repeated the spectral analysis of the sources in the 2–7 keV rest-frame band in order to check the variability of the power-law slope, ignoring the spectral region most affected by photoelectric absorption. This analysis confirmed that the general lack of change of photon index across the high and low states in the majority of the sources is not due to local absorbers. The steeper-when-brighter trend found for source 337 in the time-resolved spectral analysis is reflected in the flux-resolved spectral analysis as a slightly steeper spectrum in the high-flux state, albeit the two values are consistent within the uncertainties (see Col. 4 of Table 2).

For those sources where we observed an excess with respect to the baseline model in the soft X-rays, we have introduced additional spectral components to model such emission. Several processes can contribute to the observed soft X-rays. One possibility is that the soft excess is due to Compton up-scattering of the disc photons as described in [Done et al. \(2012\)](#). The NLR can also produce radiation in the soft X-rays as a thermal emission (that we can model through a mekal component in xspec, as was made in [Corral et al. 2008](#)). In some nearby AGN it is

often possible to detect a significant host galaxy emission, also fitted by a mekal, which may contribute to the observed soft X-ray emission (e.g. [Hernández-García et al. 2016](#)). In our sample, the soft excess is required to fit the spectra of three sources (292, 358, 48) and it has been equally well modelled by the thermal emission and by a scattering component. For source 292 this feature is detected in the high state only, perhaps because of its better counts statistics (adding such a component in the fit of the low-state spectrum does not improve the χ^2). In sources 358 and 48 it is detected in both high- and low-flux states.

The high- and low-flux states allowed us to determine the EW of the narrow iron line that was unconstrained in the individual epochs due to the insufficient statistics. A decreasing EW with an increasing luminosity, found for the first time in [Iwasawa & Taniguchi \(1993\)](#), has been explained considering that an active nucleus might blow material (where the iron line originates) away through thermal dissipation or a strong radiation pressure. Narrow iron lines have been searched for the spectra merged in the high- and low-flux states to check whether the EW is lower in high-flux states. In sources 319 and 337 they are compatible across the high and low state. In a few other sources (203, 33, and 352) instead, the lines are detected only in the low-flux state because the EW uncertainties (90% confidence level) exclude the zero value. In the same sources, the high-flux states can only give upper limits to the EW. Since the high-state spectra are characterised by typically better statistics, the lack of the line feature is not due to an insufficient spectral quality but it is an intrinsic property of those spectra and may be explained as line dilution by the intrinsic continuum in the high-flux states. For the remaining sources (292, 358, 359, 48, 382) the line could not be detected. The addition of a relativistic iron line, expected in the accretion disc scenario, to the narrow line just discussed is not required to fit the data (in all the sources) because a better spectral quality is needed to reduce the uncertainty on the continuum below the line.

The X-ray variability has provided interesting clues not only to the central engine of AGN but also on their circum-nuclear material. For instance [Risaliti et al. \(2002, 2010\)](#) and [Torricelli-Ciamponi et al. \(2014\)](#) found variations in the absorber column densities in nearby AGNs when analysing the photoelectric absorption features in their spectra. This has helped to assess the morphological properties of the absorber, supporting its clumpy structure (e.g. [Risaliti et al. 2010](#)) and constraining the recurrence cycle of BLR eclipses ([Torricelli-Ciamponi et al. 2014](#)). According to the X-ray spectral analysis, only three sources in our sample (358, 48, 352) are moderately absorbed with column density in the same range covered by [Torricelli-Ciamponi et al. \(2014; \$1-7 \times 10^{23} \text{ cm}^{-2}\$ \), while the rest of the sources do not display any significant absorption. Source 352 displays some evidence for an \$N_{\text{H}}\$ change between the high and low state \(see Table 2\) but the large uncertainties on the fit parameters \(\$N_{\text{H}}\$ and power-law photon index\) do not allow us to draw any robust conclusion on its \$N_{\text{H}}\$ variability. Amongst the sources where we do detect absorption, we do not find reliable evidence for \$N_{\text{H}}\$ variations between high and low states nor in the spectra of the individual epochs. While this can be an effect of the limited statistics and of the insufficient spectral quality, it is also possible that the timescales explored here do not allow for the observation of such variability. Indeed, our months-years timescales are longer than those of \[Torricelli-Ciamponi et al. \\(2014; which go from minutes to months\\), and this may prevent the detection of fast \\$N_{\text{H}}\\$ changes detected in those studies. Moreover, it is not surprising that our sample lacks the \\$N_{\text{H}}\\$ variations that were detected in \\[Torricelli-Ciamponi et al. \\\(2014\\\)\\]\\(#\\), since we\]\(#\)](#)

have only three candidate absorbed sources, so our sample is biased toward bright, unabsorbed AGNs.

In a few strongly absorbed AGN observed by *Chandra*, it has been possible to detect column density variability: Yang et al. (2016) studied the 68 brightest sources in the 6 Ms CDFS and found one strongly absorbed AGN with remarkable variability in the absorber (J033218.3-275055 in the *Chandra* sample). The source, with a column density of $3 \times 10^{23} \text{cm}^{-2}$ and a photon index of 1.2, is classified as a Compton Thick. Yang et al. (2016) also found a source with transitions from an obscured to an unobscured state interpreted as an eclipse event (J033229.9-274530 in that sample). In Yang et al. (2016), two more sources are found to be variable (J033226.5-274035, J033259.7-274626 in that sample), but their spectral variability is less strong than the flux variability, which is instead very significant across the *Chandra* epochs. These sources are not included within the ten AGN with the largest number of counts in the XMM-CDFS investigated in the present work.

We have explored the possibility of detecting the Compton reflection component in the spectra of the three sources with X-ray absorption (358, 352, and 48). While for source 358 the Compton reflection component is not required by the data (it does not improve the chi square), it is required in sources 352 and 48 (see the chi square and the degrees of freedom in Col. 7 of Table 2), in agreement with their HR values, ranging from 0.5 and 1 (see Figs. 10 and 11). The reflection component is not variable and its non-variability is consistent with emission from material located far away from the central SMBH. Low redshift AGN with high quality spectra show similar results; for instance a constant Compton reflection with a highly variable primary power law was found in the nucleus of the Seyfert 1 NGC 4051 (Lamer et al. 2003).

4. Summary and conclusions

We studied the X-ray spectral and flux variability of a sample of AGN detected in the XMM observations of the CDFS. We assessed the flux variability of the sources constructing the MOS1 and MOS2 lightcurves. We estimated the excess variance and the variability probability using monte-carlo simulations. A preliminary assessment of the spectral variability of each source was done examining the single-epoch HR in each epoch and looking for a correlation between HR and flux. We then performed a more refined spectral analysis merging the spectra in six epochs as well as merging the spectra of high- and low-flux states. The analysis allowed us to check if the detected variability is due to intrinsic changes in the normalisation of the power-law continuum, to changes in its slope, or to changes in the column densities of the absorber along the line of sight. We additionally explored whether we could detect the 6.4 keV iron line and if it was variable as well. We then assessed the presence (and variability) of any soft excess and we measured the contribution of a possible Compton reflection component.

Our main result is that most of the variability is due to intrinsic flux changes, related to continuum normalisation changes, but the main spectral components (e.g. power-law continuum slopes, N_{H} , iron line equivalent width) are mostly constant or marginally variable. This confirms previous results on AGN up to redshift ~ 3.5 , in several deep fields, from the first observations of the CDFS studied by Paolillo et al. (2004) to the most recent observations of the same field by Paolillo et al. (2017), as well as the LH field studied by Mateos et al. (2007), which shows that only a minority (15–20%) of the sources display spectral variability on months-years timescales. Similarly, Yang et al. (2016)

find significant evidence for strongly variable column densities in only two out of 68 sources selected from the *Chandra* CDFS survey.

The conclusions of this study can be summarised as follows:

- All the sources investigated here show significant flux variability (with a confidence level $\geq 99\%$). The lowest significance of flux variability, 99% confidence level, is found for the source with less spectral counts (source 352). This confirms that AGN are typically variable in the X-ray band over timescales of months-years and that their variability is detectable when good enough statistics are available.
- There is no strong evidence of spectral variability from the HR.
- The power-law photon index variability in this sample is found less commonly than the flux variability. We found one source with photon index variability (source 337) that displays a “softer-when-brighter” trend. The result is found on the basis of the HR study and on the spectral analysis. We do not find any source showing significant evidence for the opposite trend. The low fraction of spectrally variable sources is not expected to be intrinsic, since the spectral variability has been found in ensemble analyses (Gibson & Brandt 2012; Serafinelli et al. 2017). Indeed, its detection can potentially increase with the sample statistics as well as with the counts statistics.
- There is no significant evidence of absorption variability across the six epochs or between the high and low states. Thus, column density changes do not explain the bulk of the flux variability observed in this study.
- The narrow iron line is detected in both the high- and low-flux states (with compatible EW) for two sources (319, 337). In three sources (203, 33, 352) the narrow line is detected only in the low state. The lower iron line EW for higher continuum luminosities can be explained as an effect of line dilution by the intrinsic continuum.
- The Compton reflection component is needed to fit the spectra of two sources (352 and 48), which have very high HR. We did not find any variability of this component as expected if the reflection arises in material distributed at large distances from the central engine.
- A soft excess component is required to fit the spectra of three sources (292, 48, and 358). They are equally well-fitted by a Bremsstrahlung plus line components, which represents the emission from the NLR, or by a scattering component (a simple power law). We do not find any significant evidence for variability of this component as expected if it is emitted in material located far away from the central core.

We conclude that the flux variability is a common feature of the brightest or unabsorbed AGNs while the spectral variability is less strong. Thus, the bulk of the observed variability cannot be ascribed to changes in the primary emission mechanism nor to variations in the intervening absorbing material, but to variations in the normalisation of the primary power-law continuum.

Acknowledgements. This work is based on observations by *XMM-Newton*, an ESA science mission with instruments and contributions directly funded by ESA member states and NASA. We acknowledge the referee for useful suggestions. S.F. acknowledges the Swedish National Space Board and the Knut & Alice Wallenberg Foundation. S.F. also acknowledges the group of Particle and Astroparticle Physics and the students of the KTH for raising interesting questions about this work. F.J.C. acknowledges financial support through grant AYA2015-64346-C2-1P (MINECO/FEDER).

References

- Allevato, V., Paolillo, M., Papadakis, I., & Pinto, C. 2013, *ApJ*, **771**, 9
- Almaini, O., Lawrence, A., Shanks, T., et al. 2000, *MNRAS*, **315**, 325
- Bauer, F. E., Brandt, W. N., & Lehmer, B. 2003, *AJ*, **126**, 2797
- Belloni, T., Méndez, M., King, A. R., van der Klis, M., & van Paradijs, J. 1997, *ApJ*, **488**, L109
- Comastri, A., Ranalli, P., Iwasawa, K., et al. 2011, *A&A*, **526**, L9
- Corral, A., Page, M. J., Carrera, F. J., et al. 2008, *A&A*, **492**, 71
- Done, C., Davis, S. W., Jin, C., Blaes, O., & Ward, M. 2012, *MNRAS*, **420**, 1848
- Edelson, R. A., Alexander, T., Crenshaw, D. M., et al. 1996, *ApJ*, **470**, 364
- Edelson, R., Turner, T. J., Pounds, K., et al. 2002, *ApJ*, **568**, 610
- Esin, A. A., McClintock, J. E., & Narayan, R. 1997, *ApJ*, **489**, 865
- Fender, R., & Belloni, T. 2004, *ARA&A*, **42**, 317
- Georgantopoulos, I., Comastri, A., Vignali, C., et al. 2013, *A&A*, **555**, A43
- Gibson, R. R., & Brandt, W. N. 2012, *ApJ*, **746**, 54
- Hernández-García, L., Masegosa, J., González-Martín, O., Márquez, I., & Perea, J. 2016, *ApJ*, **824**, 7
- Iwasawa, K., & Taniguchi, Y. 1993, *ApJ*, **413**, L15
- Iwasawa, K., Mainieri, V., Brusa, M., et al. 2012, *A&A*, **537**, A86
- Iwasawa, K., Vignali, C., Comastri, A., et al. 2015, *A&A*, **574**, A144
- Komatsu, E., Smith, K. M., Dunkley, J., et al. 2011, *ApJS*, **192**, 18
- Lamer, G., McHardy, I. M., Uttley, P., & Jahoda, K. 2003, *MNRAS*, **338**, 323
- Lanzuisi, G., Ponti, G., Salvato, M., et al. 2014, *ApJ*, **781**, 105
- Luo, B., Brandt, W. N., Xue, Y. Q., et al. 2017, *ApJS*, **228**, 2
- Malizia, A., Bassani, L., Stephen, J. B., Malaguti, G., & Palumbo, G. G. C. 1997, *ApJS*, **113**, 311
- Mateos, S., Barcons, X., Carrera, F. J., et al. 2007, *A&A*, **473**, 105
- McHardy, I. M., Koerding, E., Knigge, C., Uttley, P., & Fender, R. P. 2006, *Nature*, **444**, 730
- Middei, R., Vagnetti, F., Bianchi, S., et al. 2017, *A&A*, **599**, A82
- Nandra, K., George, I. M., Mushotzky, R. F., Turner, T. J., & Yaqoob, T. 1997, *ApJ*, **476**, 70
- Paolillo, M., Schreier, E. J., Giacconi, R., Koekemoer, A. M., & Groggin, N. A. 2004, *ApJ*, **611**, 93
- Paolillo, M., Pinto, C., Giacconi, R., et al. 2007, in *X-ray Surveys, Evolution of Accretion, Star-Formation and the Large Scale Structure*, 23
- Paolillo, M., Papadakis, I., Brandt, W. N., et al. 2017, *MNRAS*, **471**, 4398
- Papadakis, I. E., Sobolewska, M., Arevalo, P., et al. 2009, *A&A*, **494**, 905
- Park, T., Kashyap, V. L., Siemiginowska, A., et al. 2006, *ApJ*, **652**, 610
- Puccetti, S., Risaliti, G., Fiore, F., et al. 2004, *Nucl. Phys. B Proc. Suppl.*, **132**, 225
- Ranalli, P., Comastri, A., Vignali, C., et al. 2013, *A&A*, **555**, A42
- Rees, M. J. 1984, *ARA&A*, **22**, 471
- Risaliti, G., Elvis, M., & Nicastro, F. 2002, *ApJ*, **571**, 234
- Risaliti, G., Elvis, M., Bianchi, S., & Matt, G. 2010, *MNRAS*, **406**, L20
- Serafinelli, R., Vagnetti, F., & Middei, R. 2017, *A&A*, **600**, A101
- Shemmer, O., Brandt, W. N., Paolillo, M., et al. 2014, *ApJ*, **783**, 116
- Silverman, J. D., Mainieri, V., Salvato, M., et al. 2010, *ApJS*, **191**, 124
- Sobolewska, M. A., & Papadakis, I. E. 2009, *MNRAS*, **399**, 1597
- Szokoly, G. P., Bergeron, J., Hasinger, G., et al. 2004, *ApJS*, **155**, 271
- Torricelli-Ciamponi, G., Pietrini, P., Risaliti, G., & Salvati, M. 2014, *MNRAS*, **442**, 2116
- Treister, E., Virani, S., Gawiser, E., et al. 2009, *ApJ*, **693**, 1713
- Turner, T. J., George, I. M., Nandra, K., & Turcan, D. 1999, *ApJ*, **524**, 667
- Vagnetti, F., Middei, R., Antonucci, M., Paolillo, M., & Serafinelli, R. 2016, *A&A*, **593**, A55
- Vaughan, S., Edelson, R., Warwick, R. S., & Uttley, P. 2003, *MNRAS*, **345**, 1271
- Vignali, C., Iwasawa, K., Comastri, A., et al. 2015, *A&A*, **583**, A141
- Yang, G., Brandt, W. N., Luo, B., et al. 2016, *ApJ*, **831**, 145
- Young, M., Brandt, W. N., Xue, Y. Q., et al. 2012, *ApJ*, **748**, 124
- Zdziarski, A. A., Lubiński, P., & Smith, D. A. 1999, *MNRAS*, **303**, L11
- Zdziarski, A. A., Lubiński, P., Gilfanov, M., & Revnivtsev, M. 2003, *MNRAS*, **342**, 355
- Zoghbi, A., Fabian, A. C., Reynolds, C. S., & Cackett, E. M. 2012, *MNRAS*, **422**, 129